Research Square

Preprints are preliminary reports that have not undergone peer review.
They should not be considered conclusive, used to inform clinical practice,
or referenced by the media as validated information.

Progressive endothelial dysfunction and endothelial-to-mesenchymal transition in cerebral cavernous malformations

Monica Gallego-Bonhomme
Spanish National Research Council (CSIC)
Anna Lopresti-Vega
Hospital Universitario Fundación Jiménez Díaz
Alfonso Lagares-Gómez
Hospital Universitario 12 Octubre
Ana-María Castaño
Hospital Universitario 12 Octubre
Alejandra Cue-Avello
Spanish National Research Council (CSIC)
Raul Iglesias-Belles
Spanish National Research Council (CSIC)
Laura Lorente-Herraiz
Spanish National Research Council (CSIC)
Lucia Recio-Poveda
Spanish National Research Council (CSIC)
Sheila Pinto-García
Centre for Biomedical Network Research on Rare Diseases
Jesus Viñas-Lopez
Secugen,S.L
Angel M Cuesta
Universidad Complutense de Madrid
Luisa M Botella
Spanish National Research Council (CSIC)
Virginia Albiñana
viralbidi@cib.csic.es

Spanish National Research Council (CSIC)

Research Article

Keywords: Cerebral cavernous malformations, Endothelial-to-mesenchymal transition, Endothelial dysfunction, Angiogenesis, PI3K/mTOR signaling, Blood outgrowth endothelial cells

Posted Date: September 11th, 2026

DOI: https://doi.org/10.21203/rs.3.rs-10878315/v1

License: This work is licensed under a Creative Commons Attribution 4.0 International License.
Read Full License

Additional Declarations: No competing interests reported.

Progressive endothelial dysfunction and endothelial-to-mesenchymal transition in cerebral cavernous malformations

Monica Gallego-Bonhomme[1], Anna Lopresti-Vega[2], Alfonso Lagares-Gomez[3], Ana M Castaño[3], Alejandra Cue-Avello[1] , Raul Iglesias-Belles[1] , Laura Lorente-Herraiz[1,4], Lucía Recio-Poveda[1,4], Sheila Pinto-Garcia[1,4] , Jesús Viñas-López[5] Ángel M Cuesta[4,6], Luisa-María Botella[1,4,*] Virginia Albiñana[1,4*]

[1]Margarita Salas Center for Biological Research (CIB-CSIC), Spanish National Research Council (CSIC), Madrid, Spain: monica8gb@gmail.com ,alecue8@gmail.com, Raul.Iglesias@alu.uclm.es, laura.lorente@cib.csic.es, lrecio@cib.csic.es, spinto@cib.csic.es, viralbidi@cib.csic.es, , cibluisa@cib.csic.es,

[2]Neurosurgery Department, Institute of Health Research. Jiménez Díaz Foundation. University Hospital, Madrid, Spain; alopresti@fjd.es.

[3]Neurosurgery Department Hospital Universitario 12 Octubre Madrid. Spain: alfonso.lagares@salud.madrid.org, ana.castano@salud.madrid.org

[4]U-707. Spanish Network of Biomedical Research on Rare Diseases (CIBERER), 28040 Madrid, Spain.

[5] Secugen,S.L. Sequencing and molecular diagnosis. Madrid, Spain; j.vinas@secugen.es.

[6] Biochemistry and Molecular Biology Department. Faculty of Pharmacy. Complutense University of Madrid. 28040 Madrid, Spain; angcuest@ucm.es.

* Correspondence: cibluisa@cib.csic.es and viralbidi@cib.csic.es

Graphical Abstract. Familial CCM endothelial cells and cavernoma-derived cells share a common process, endothelial-to-mesenchymal transition (EndMT). The color gradient reflects EndMT progression, from endothelial (blue) to partial (green) and to advanced transition (red). Heterozygous FCCM endothelial cells (*KRIT1*-/+) and cavernoma-derived cells, which also carry a somatic second hit and, in most cases, a *PIK3CA* mutation, sit at different points of this gradient, showing loss of endothelial markers, gain of mesenchymal ones, increased viability, and impaired wound healing and tubulogenesis. In FCCM cells, two strategies were tested *in vitro* to limit cavernoma growth and bleeding: β-adrenergic blockade and PI3K/AKT/mTORC1 inhibition.

ABSTRACT

Background: Cerebral cavernous malformations (CCMs) are vascular lesions of the central nervous system caused by germline mutations in *KRIT1*, *CCM2*, or *PDCD10* in familial disease (FCCM) and by somatic mutations in sporadic CCM (SpCCM). Endothelial-to-mesenchymal transition (EndMT) and PI3K/mTOR activation have been implicated in lesion growth, but whether endothelial dysfunction precedes lesion formation remains unclear.

Methods: We studied blood outgrowth endothelial cells (BOECs) from three siblings of a CCM1 family, including two heterozygous mutation carriers and one wild-type sibling, and primary cells isolated from resected FCCM and SpCCM lesions. Cells were studied by DNA sequencing, functional assays, RT-qPCR, and protein analysis. FCCM cells were also exposed in vitro to PI3K/mTOR and β-adrenergic inhibitors as candidate repurposed drugs.

Results: BOECs from heterozygous carriers showed reduced endothelial identity and impaired

migration and angiogenic capacity. Differences between carriers were associated with additional variants present ineach sibling. FCCM and SpCCM cells carrying mutations in CCM genes and *PIK3CA*, respectively, showed progressive loss of endothelial markers, increased mesenchymal markers, and disorganized actin cytoskeleton, consistent with an EndMT-like phenotype.

Conclusions: These findings identify progressive endothelial dysfunction and an EndMT-like phenotype as shared features of familial and sporadic CCM and support patient-derived endothelial models as platforms for investigating disease mechanisms and potential therapeutic strategies.

KEY WORDS: Cerebral cavernous malformations; Endothelial-to-mesenchymal transition; Endothelial dysfunction; Angiogenesis; PI3K/mTOR signaling; Blood outgrowth endothelial cells

INTRODUCTION

Cerebral cavernous malformations (CCMs), also known as cavernomas, are vascular anomalies of the central nervous system (CNS) affecting approximately 0.16–0.4% of the general population [1–3]. They are the second most common CNS vascular malformation and an important cause of stroke, seizures, and neurological disability, particularly in younger individuals [4,5]. Although often asymptomatic and incidentally discovered, CCMs may present with intracerebral hemorrhage, epilepsy, headaches, or focal neurological deficits [4–6].

Histologically, CCMs consist of clusters of dilated capillary-like vessels lined by endothelial cells lacking normal tight junctions and smooth muscle or elastic layers [7]. These fragile vessels are prone to leakage and are typically surrounded by hemosiderin deposits and gliosis, with little or no intervening neural tissue. Endothelial hyperpermeability, blood–brain barrier disruption, inflammation, and dysregulated angiogenesis are key features of CCM pathophysiology and contribute to lesion instability and hemorrhagic risk [4,7].

Familial CCMs, which account for approximately 15% of cases, are caused by germline loss-of-function mutations in one of three CCM genes: *CCM1(KRIT1*), *CCM2 (malcavernin*), or *CCM3* (*PDCD10*). These proteins form the CCM signaling complex (CSC), a critical regulator of endothelial homeostasis that integrates cell–cell adhesion, cytoskeletal organization, and vascular signaling [8–10]. Through interactions with the VE-cadherin/β-catenin complex and regulation of the Rho/Rac pathway, the CSC contributes to endothelial junctional integrity and cytoskeletal stability, while its negative regulation of the MEKK3-KLF2/4 pathway restrains endothelial activation and maintains vascular homeostasis [11-13]. Despite the genetic basis, familial CCMs display marked phenotype heterogeneity in disease severity, suggesting a role for modifying genomic and environmental factors [14–16]. Most CCMs are sporadic, typically presenting as isolated lesions [5,17]. For many years, the genetic basis of sporadic CCMs remained unclear, as pathogenic variants in the CCM genes were detected only in low percentage of the cavernous cells [18,19]. Recent advances in deep, massive sequencing have improved the identification of somatic mutations arising within CCM endothelial cells [20,21]. In sporadic CCMs, somatic loss-of-function mutations in the same pathway can similarly initiate lesion development, with additional activating mutations, particularly in *PIK3CA* or *MAP3K3*, promoting endothelial proliferation, cytoskeletal remodeling, and vascular permeability [22-26]. Thus, irrespective of their familial or sporadic origin, CCMs converge on the disruption of endothelial homeostasis, providing a mechanistic link to the endothelial phenotypic changes that precede and accompany EndMT.

The discovery of *PIK3CA*-mediated mTOR pathway hyperactivation as a central growth mechanism in a high proportion of CCMs has important therapeutic implications. Preclinical studies have shown that pharmacological inhibition of mTORC1 with rapamycin effectively suppresses lesion growth in mouse models of human sporadic CCM, even in the adult brain [22-28]. These findings suggest that targeted medical therapies may represent a viable adjuvant alternative to surgery, particularly for patients with inoperable lesions.

Despite these advances, substantial clinical, genomic, and histopathologic heterogeneity persists among CCMs, and the determinants of lesion behavior and stroke risk remain incompletely defined [29-31]. Integrating molecular profiling with clinical and MRI phenotypes is therefore essential to anticipate CCM-related risk. To this end, the identification of biomarkers of hemorrhage and epilepsy, as well as the development of personalized, precision therapies for CCM patients, are pressing needs. Such efforts are critical to reducing stroke-related morbidity and advancing individualized management strategies in this complex cerebrovascular disorder.

Moreover, endothelial features were found to be substantially disrupted in cells from both familial and sporadic cavernomatous lesions. Cells derived from the lesions had undergone endothelial-to-mesenchymal transition (EndMT), characterized by the loss of endothelial markers and the gain of mesenchymal markers. Most notably, the vascular cells from normal vessels in familial cavernomatosis patients, already showed the onset of this transition, reinforcing results previously published by our group [32].

The present work provides a molecular and functional characterization of endothelial dysfunction in CCM patients at three levels. First, we characterized blood outgrowth endothelial cells (BOECs) obtained from three siblings of a CCM1 family. These cells are derived from the in vitro expansion of circulating endothelial progenitor cells of bone marrow origin and therefore represent heterozygous endothelial cells. Second, we performed a molecular and functional study of cells grown from the surgical remnant of a CCM1 hereditary cavernous lesion. Finally, to complete the CCM scenario, we analyzed cells derived from an isolated sporadic cavernoma.

Here, we investigated whether endothelial dysfunction is detectable in apparently non-lesional endothelial cells from individuals carrying a heterozygous *KRIT1* mutation and whether this phenotype progresses toward an EndMT-like state in endothelial cells derived from familial and sporadic CCM lesions. We further explored whether PI3K/mTOR and β-adrenergic pathways represent potentially targetable features of CCM-derived endothelial cells.

MATERIALS AND METHODS

Ethics Approval and Consent to Participate

All procedures were performed in compliance with the guidelines and regulations established by the Consejo Superior de Investigaciones Científicas (CSIC) and Spanish national legislation. Experimental protocols involving human samples were approved by the CSIC Ethical Committee (reference numbers 228/2020 and 126/2024 corresponding to grants PID2020-115371RB-I00 and PID2023-1465930B-I00, respectively) and conducted in accordance with the principles set forth in the Declaration of Helsinki of the World Medical Assembly. Written informed consent was obtained from all patients whose surgical surplus tissue was used for the generation of primary cultures.

Genetic characterization

The library preparation was designed using SureSelectXT technology (Agilent Technologies), targeting the capture of the exons of the genes of interest and the flanking splicing regions (5–20 bp). Sequencing of the library was performed using an Illumina next-generation high-throughput sequencer. The sequences obtained were aligned against the reference genome (GRCh37/hg19) and filtered according to specific quality criteria.

Subsequently, the data were analyzed to identify genetic variants located within exonic regions or splicing regions (at least 5 bp), including missense and nonsense mutations, synonymous variants, indels, and small insertions or deletions with a variant allele frequency (VAF) greater than 5% of the reads. Variant annotation was performed using VarSome software version 13.1.2 (updated on 27/02/2025).

As part of this analysis, changes across all genes in the whole exome were evaluated using specific filters for pathogenic or likely pathogenic variants, as well as for variants that did not meet the quality criteria for allelic balance below 5%.

The mean coverage obtained was 460× across the target regions, with 99% of the regions sequenced at a depth of at least 20× and a coverage uniformity of 93.56%. The percentage of Q30 bases obtained was 91.65%.

Data were analyzed to identify genetic variants located within exonic regions or splicing regions (at least 5 bp), including missense and nonsense mutations, synonymous variants, indels, and small insertions or deletions with a variant allele frequency (VAF) greater than 5% of the reads. Both processes were carried out using the DRAGEN™ BioIT Platform (Illumina, version 07.021.510.3.5.7).

Cell Culture

BOECs (Blood Outgrowth Endothelial Cells) were cultured from 50 mL of peripheral blood obtained from volunteers after reading and signing a written informed consent form. Blood samples from CCM patients were processed by Ficoll density-gradient centrifugation: samples were diluted 1:1 in HBSS and transferred to a 50 mL tube containing 25 mL of Lymphoprep™. After centrifugation for 30 minutes at 1750 rpm without acceleration or braking, the peripheral blood mononuclear cell (PBMC) halo was collected, washed, and seeded onto collagen-coated 6-well plates (plates were washed twice with HBSS to remove excess collagen before use). Cells were maintained in Endothelial Growth Medium-2 (EGM-2; Lonza, Walkersville, MD, USA) supplemented with 20% FBS, 2 mM L-glutamine, and 100 U/mL

penicillin/streptomycin (GIBCO, Grand Island, NY, USA).

Primary cultures of cavernoma cells were established from small surgical remnants of a familial (FCCM) and a sporadic (SpCCM) cavernoma, following written informed consent from all participants. Samples were rinsed repeatedly with PBS and sectioned into 1 mm^3 fragments. Tissue pieces were transferred with sterile tweezers to clean culture dishes (Sarstedt, Germany) and enzymatically dissociated with an equal volume of collagenase I for 15 minutes at 37°C. The resulting cell suspension was centrifuged, and the pellet was resuspended in EGM-2 supplemented with 20% FBS, 1% penicillin/streptomycin, and 4 mM glutamine, and maintained at 37°C. The medium was refreshed every 48 hours until confluence was reached. All endothelial cells used in this study (Human Umbilical Vein Endothelial Cells (HUVECs), BOECs, and cavernoma-derived cells (FCCM and SpCCM)), were cultured in EGM-2 medium under the conditions described above.

Cell Viability Assay

Cell viability was assessed using the CellTiter-Glo Luminescent Cell Viability Assay kit (Promega, Madison, WI, USA), a homogeneous quantitative method that determines the number of viable cells in culture through ATP quantification, reflecting metabolically active cells. Briefly, 5×10^3 cells/well (healthy BOECs, FCCM, or SpCCM) were plated in 96-well plates and maintained in complete medium supplemented with increasing concentrations (0–100 µM) of propranolol, ICI-118,551, buparlisib, or rapamycin for the duration indicated in each experiment. Subsequently, 100 µL/well of CellTiter-Glo reagent was added, and plates were gently agitated for 15 minutes at room temperature. Luminescence was recorded using a GloMax Multidetection System (Promega, Madison, WI, USA).

Tubulogenesis Assay

Matrigel Matrix (BD Biosciences, Bedford, MA, USA), diluted 1:1 in plain DMEM (GIBCO), was used to coat 24-well plates (150 µL/well). After 30 minutes, 8×10^5 cells were seeded and cultured in EGM-2. Images were taken from 1.5 hours after seeding and up to 6 hours thereafter using an Olympus digital

camera. Quantification of the tube network formed in each condition was performed using GIMP 2.10 software (UC Berkeley, Berkeley, CA, USA).

Wound Healing Assay

Cell migration was assessed by an *in vitro* wound-healing assay. Once confluence was reached in a 24-well plate, the cell monolayer was scratched with a 200 µL pipette tip to create a gap (wound) in each well. After washing with PBS and adding fresh EGM-2, wound closure was monitored between 0 and 6.5 hours post-wounding. Images were taken with an Olympus digital camera and analyzed using GIMP 2.10 software (UC Berkeley).

Real-Time RT-qPCR

Total RNA was isolated using the NucleoSpin RNA kit (Macherey-Nagel, Düren, Germany). One microgram of total RNA was reverse-transcribed into cDNA in a final volume of 20 µL using the High-Capacity cDNA Reverse Transcription Kit (Applied Biosystems) with random primers. Real-time PCR was performed using the SYBR Green PCR system (Roche) on an iQ5 platform (BioRad, Hercules, CA, USA), with 18S rRNA used as the internal reference for normalization. All samples were run in triplicate.

Table 1. Primer sequences used for RT-qPCR.

18S	CTCAACACGGGAAACCTCAC	CGCTCCACCAACTAAGAACG
aSMA	CTATGCCTCTGGACGCACAACT	CAGATCCAGACGCATGATGGCAT
ANGPT2	TGCAAATGTTCACAAATGCTAA	AAGTTGGAAGGACCACATGC
BCL2	TACTGGCCTTGGCTGTGCT	CACAGGGTTTTCACCAACCT
CAT	CTCCGGAACAACAGCCTTC	ATAGAATGCCCGCACCTG
CCNB2	TGGAAAAGTTGGCTCCAAAG	CTTCCTTCATGGAGACATCCTC
CDH2	CCTCCAGAGTTTACTGCCATGAC	GTAGGATCTCCGCCACTGATTC
CDH5	GGAGGAGCTCACTGTGGATT	CTGATGCAGCAAGGACAGC
ENG	AGCCACATCGCTCAGACAC	GCCAATACGACCAAATCC
FN1	TCCATTACCAAGACACACACACT	GGGAGAATAAGCTGTACCATCG
FSP1	CAGAACTAAAGGAGCTGCTGACC	CTTGGAAGTCCACCTCGTTGTC
FVW	GATGGTGCTTCGGTGGAC	TGGGTACTTGGCCTCAACC
IL6	GAAGGCAGCAGGCAACAC	CAGGAGCCCAGCTATGAACT
KDR	GAGTGAGGAAGGAGGACGAAGG	CCGTAGGATGATGACAAGAAGTAGC
KLF4	CATCTCAAGGCACACCTGCGAA	TCGGTCGCATTTTTGGCACTGG
KRIT1	CTGTAAGAACATGCGCTGAAG	TCCATCGTACCTGTTACCAAAC
MKI67	GAAAGAGTGGCAACCTGCCTTC	GCACCAAGTTTTACTACATCTGCC

MMP3	CACTCACAGACCTGACTCGGTT	AAGCAGGATCACAGTTGGCTGG
NOS-3	GACCCTCACCGCTACAACAT	CCGGGTATCCAGGTCCAT
PECAM1	AGAAAACCACTGCAGAGTACCAG	GGCCTCTTTCTTGTCCAGTGT
PTGS2	TCACGCATCAGTTTTTCAAGA	TCACCGTAAATATGATTTAAGTCCAC
SERPINE1	TCCAGCACGTGAATTCCTG	GTCGGAGACATCTGCATCCT
SNAI1	TGCCCTCAAGATGCACATCCGA	GGGACAGGAGAAGGGCTTCTC
SOD2	AACACCTCCCTACGCCAAC	TCCCTCGTGCTTGGATTG
VIM	GAGAACTTTGCCGTTGAAGC	GCTTCCTGTAGGTGGCAATC

Immunofluorescence

Immunofluorescence assays were performed to visualize CD31, VE-cadherin, F-actin, and γ-tubulin. Cells were seeded at a density of 50,000 cells/well onto collagen-coated circular coverslips in 24-well plates and incubated at 37°C for 24 h to allow adherence. Each marker was analyzed in triplicate using independent coverslips. Cells were washed with cold 1× PBS, fixed with 3.5% PFA for 20 min at room temperature, and blocked with 1× PBS containing 1% BSA for 45 min. Cells were then incubated with an Alexa Fluor 647-conjugated anti-CD31 antibody (Invitrogen), an anti-VE-cadherin antibody (Sigma-Aldrich), or an anti-γ-tubulin antibody (Sigma-Aldrich) in a humidified chamber at room temperature for 40 min. F-actin was stained with Alexa Fluor 547-conjugated phalloidin (Invitrogen). After incubation with the primary antibodies and extensive washes with PBS, the corresponding samples were incubated for 30 min with Alexa Fluor 488/547 secondary antibodies. Coverslips were then washed with 1× PBS and mounted onto glass slides using Prolong Gold Antifade Mountant with DAPI (Invitrogen). Samples were stored at -20ºC until imaging with an SP5 confocal microscope (Leica Microsystems).

Western Blot

Protein extraction was performed using TNE lysis buffer (50 mM Tris, 150 mM NaCl, 1 mM EDTA, 0.5% Triton X-100) supplemented with protease and phosphatase inhibitors (Roche) and the proteasome inhibitor lactacystin (Sigma-Aldrich). Lysates were centrifuged for 5 minutes, and protein concentration was determined by the Bradford assay using Coomassie Brilliant Blue reagent (Promega). Equal amounts of protein were boiled in SDS sample buffer and resolved on precast 4–20% gradient SDS-PAGE gels (BioRad) under reducing conditions. Proteins were transferred onto nitrocellulose membranes (Amersham, Little Chalfont, UK) by overnight electrotransfer. Membranes were blocked with 5% BSA in TBS-0.05% Tween for 1 hour at room temperature and then incubated overnight at 4°C with primary antibodies against VE-cadherin (1:500), CCM1 (Abcam) (1:500), or γ-tubulin (1:10,000; mouse mAb, Sigma-Aldrich). Membranes were washed with TBS-0.05% Tween-20 and incubated with the corresponding HRP-conjugated secondary antibody (1:2000) (Dako, Glostrup, Denmark) for 1 hour at room temperature. After further washes, membranes were developed by chemiluminescence (SuperSignal West Pico Chemiluminescent Substrate, Thermo Scientific), and band intensity was quantified using FIJI-ImageJ software.

Statistics

All experiments were performed at least three independent times. Data are presented as mean ± standard deviation (SD). Statistical analyses were performed using GraphPad Prism 8. Depending on the experiment, data were analyzed by two-way ANOVA followed by Tukey's or Šídák's multiple comparisons test, or by an unpaired t-test with Welch's correction.

RESULTS

Familial Cerebral Cavernous Malformation Case

Blood Outgrowth Endothelial Cells (BOECs) were isolated from peripheral blood obtained from two siblings affected by familial cerebral cavernous malformation, designated patient CCMA (BOEC-A) and patient CCMB (BOEC-B). BOECs derived from a third, unaffected sibling were used as a healthy control. Genetic analysis by whole-exome sequencing at 500× coverage confirmed the presence of pathogenic familial mutations in the *KRIT1* gene in both CCMA and CCMB in heterozygous condition, and verified the absence of disease-associated alterations in the control sibling. Several additional secondary variants potentially affecting normal endothelial function were also identified in both patients (**Figure 1A**). Morphological examination of the three cell cultures revealed that BOEC-B cells displayed a clearly endothelial morphology, with the characteristic cobblestone appearance similar to control cells, whereas BOEC-A cells exhibited a markedly elongated phenotype with little resemblance to the control (**Figure 1B**).

Figure 1. Genetic and morphological characterization of patient-derived endothelial cells. (A) Variants identified by whole-exome sequencing (500×) in BOEC-A and BOEC-B, FCCM, and SpCCM cells. Variants shared by BOEC-A and BOEC-B are shown first, followed by variants identified exclusively in each sample. The table includes the gene, genomic region, variant, allele frequency, and predicted protein effect. (B) Representative brightfield images of BOEC cultures from the three siblings (Control, BOEC-A, and BOEC-B, upper row) and FCCM and SpCCM cells compared with control HUVECs (lower row).

Functional assays reveal differences between control BOECs and FCCM BOECs

To evaluate angiogenic capacity, a tube formation (tubulogenesis) assay was performed. BOEC-A cells were virtually incapable of forming closed tubes and failed to organize into tube-like structures. In contrast, BOEC-B cells exhibited normal tubulogenic capacity, forming a number of closed tubes comparable to that of control cells at both time points evaluated (**Figure 2A**).

A wound-closure assay was performed to assess cell migratory capacity. BOEC-B cells displayed a migratory behavior similar to that of control cells, reaching comparable wound-closure percentages at both time points evaluated. In contrast, BOEC-A cells showed significantly reduced migration compared with both control and BOEC-B, exhibiting minimal wound closure and leaving the wound area virtually unchanged from its initial size (**Figure 2B**).

Molecular Characterisation by RT-qPCR shows loss of endothelial identity in FCCM BOECs

RT-qPCR analysis revealed alterations in several genes related to endothelial identity, cell proliferation, and vascular homeostasis in BOEC-A and BOEC-B cells compared with the healthy control (Figure 2C). Overall, the expression of classical endothelial markers, including *PECAM1*, *KDR,* and *VE-cadherin*, was reduced. Similarly, the expression of genes associated with endothelial function, such as *ENG*, *NOS3*, and *ANGPT2*, was also decreased, with a more pronounced reduction for some markers,

particularly in BOEC-B. In contrast, *CCNB2* expression was markedly increased in BOEC-A, suggesting enhanced proliferative activity. *COX2* expression was virtually abolished in both mutated cell lines compared with the control. As expected, *KRIT1* expression was reduced in both patients relative to the control, consistent with the heterozygous genetic alteration. In contrast, *SERPINE1* expression was largely preserved and was even slightly increased in both BOEC-A and BOEC-B compared with the healthy control (**Figure 2C**).

Figure 2. Functional characterization of BOECs A, B, and C. A) Tubulogenesis assay. Brightfield images show tube formation by the different cell types, and the graph shows the number of closed tubes formed by each cell type over time. Error bars denote ± SD. Two-way ANOVA with Tukey's multiple comparisons test. ****p<0.0001. (B) Wound healing assay. Brightfield images show the progression of wound closure, with vertical lines indicating the position of the wound front. The graph on the right shows the percentage of wound closure over time. Error bars denote ± SD. Two-way ANOVA with Sidak's multiple comparisons test. *p<0.05, ****p<0.0001. (C) RT-qPCR analysis performed using Bio-Rad iQ5 Optical System software, with 18S as the housekeeping gene. Differential expression was observed in genes involved in endothelial function, cell cycle regulation, and inflammation. Error bars denote ± SD. Two-way ANOVA with Tukey's multiple comparisons test. *p<0.05, **p<0.01, ***p<0.001, ****p<0.0001.

Genetic and phenotypic characterisation of familial and sporadic cavernoma-derived cells.

Small surgical surplus tissue from a familial cavernoma (FCCM) and a sporadic cavernoma (SpCCM), both of which had previously bled, was obtained and analyzed by whole-exome sequencing at 500× coverage. Both, the germline pathogenic variant and the somatic second hit required for lesion development, were identified in each cavernoma. In the FCCM sample, a germline mutation in the *KRIT1* gene was identified together with a somatic second-hit mutation in the same gene. In the SpCCM sample, two somatic mutations were identified, both affecting the *CCM2* gene. Importantly, gain-of-function mutations in *PIK3CA* were detected in a low percentage of cells in both lesions, resulting in constitutive activation of the PI3K/AKT/mTOR pathway (**Figure 1A**). Activating *PIK3CA* mutations have been associated with aberrant, exacerbated cavernoma growth through mechanisms analogous to those observed in cancer, prompting us to examine the functional consequences of PI3K pathway activation in our cavernoma cell models. At the morphological level, both FCCM and SpCCM cells displayed a more elongated shape relative to the healthy control, although this phenotype was much more pronounced in FCCM cells, whereas only a small proportion of SpCCM cells exhibited this elongated morphology. (**Figure 1B**).

Functional Assays reveal marked endothelial dysfunction in FCCM and SpCCM cells

To assess whether cavernoma cells exhibited altered viability, an ATP-based cell viability assay was performed. Both FCCM and SpCCM cells showed significantly higher ATP levels than healthy endothelial cells, indicating an increased number of metabolically active cells. In FCCM cells, this increase became apparent only at the latest time point evaluated (72 h), whereas in SpCCM cells elevated ATP levels were observed at both 48 h and 72 h. (**Figure 3A**).

The tubulogenesis assay revealed marked alterations in the ability of FCCM and SpCCM cells to establish endothelial tubular networks. FCCM cells formed tubes that were more disorganized than those generated by healthy control cells. These structures were less stable and retracted more rapidly over time. In contrast, SpCCM cells were unable to establish proper tubular networks at either of the time points evaluated, forming only a few thin and poorly organized tubes. Overall, both FCCM and SpCCM cells formed significantly fewer closed tubes than healthy controls, confirming their impaired angiogenic capacity (**Figure 3B**). Regarding wound healing, the leading edge of the scratch closed

significantly slower under both the FCCM and SpCCM conditions, indicating an impaired migratory capacity and a reduced ability of the vascular endothelium to repair damage. Notably, even at 0 h, immediately after the scratch was performed, the wound edges did not present a straight front, a feature likely attributed to a loss of cell culture adherence **(Figures 3C-E).**

Figure 3. Functional characterization of FCCM and SpCCM cells. (A) Cell viability assessed by ATP quantification over time in FCCM cells compared with control BOECs (left) and SpCCM cells compared with control HUVECs (right). Error bars indicate ± SD. Two-way ANOVA with Šídák's multiple-comparisons test. *p<0.05; **p<0.01; ***p<0.001; ****p<0.0001. (B) Representative brightfield images of the tubulogenesis assay comparing control BOECs and FCCM cells (left) and control HUVECs and SpCCM cells (right) at the indicated time points. Quantification of closed tubes is shown on the right. Upper graph: control BOECs versus FCCM cells at 2.5 h, as tubes had retracted by 24 h. Error bars indicate ± SEM. Welch's t-test. **p<0.01. Lower graph: control HUVECs versus SpCCM cells at 2 and 4 h. Error bars indicate ± SD. Two-way ANOVA with Šídák's multiple-comparisons test. **p<0.01. (C) Representative brightfield images of the wound healing assay comparing control BOECs and FCCM cells at 0, 3, 5, and 9 h. Vertical lines indicate the wound edges. (D) Representative brightfield images comparing control HUVECs and SpCCM cells at 0 and 5 h. Vertical lines indicate the wound edges. (E) Quantification of wound closure. Upper graph: percentage of wound closure over time in control BOECs and FCCM cells. Error bars indicate ± SD. Two-way ANOVA with Šídák's multiple-comparisons test. ****p<0.0001. Lower graph: percentage of wound closure in control HUVECs and SpCCM cells at 9 h. Error bars indicate ± SD. Unpaired t-test with Welch's correction. **p<0.01.

Molecular Characterisation by RT-qPCR an EndMT pattern of expression in FCCM and SpCCM cells

To determine whether the transcriptional changes observed in FCCM cells evolve over time in culture, cells at low passage (passage 5, FCCM P5) and high passage (passage 11, FCCM P11) were compared with healthy BOECs, analyzing markers of endothelial identity, endothelial-to-mesenchymal transition (EndMT), and cellular homeostasis (**Figure 4A–C**).

FCCM cells showed a significant, progressive reduction in major endothelial markers, including *PECAM1, CDH5, VWF, NOS3, ENG, ANGPT2,* and *KDR*, indicating a loss of endothelial identity that was accentuated with increasing passage number (**Figure 4A**). Notably, *KRIT1* expression was elevated at high passage, which might reflect a compensatory mechanism increasing the rate of transcripts that will not be translated into the complete protein.

In parallel, a progressive overexpression of mesenchymal markers was observed, including *CDH2, FN1, KLF4, SNAI1,* and *VIM*. Most strikingly, αSMA and *FSP1* reached levels approximately 10- and 16-fold higher than in BOECs in FCCM S5 cells, confirming the acquisition of a mesenchymal phenotype at advanced culture stages (**Figure 4B**).

FCCM cells at passage 5 showed increased expression of genes associated with cell cycle progression, proliferation, and cell survival, including *CCNB2*, *MKI67*, and *BCL2*. This finding is consistent with the increased cell viability observed in the ATP-based assay. The expression of these three genes was reduced at passage 11, indicating that their upregulation was more pronounced at earlier passages. In addition, a marked decrease in *SERPINE1/PAI-1* expression was observed. Given the role of PAI-1 in the regulation of fibrinolysis, this finding may be consistent with the hemorrhagic phenotype of the resected lesions analyzed in this study. *IL6* expression was also increased, consistent with an inflammatory activation of the endothelial cells. (**Figure 4C**). Altogether, these data indicate that FCCM endothelial cells not only lose their endothelial identity and acquire mesenchymal characteristics, but also progressively compromise their cellular homeostasis over time in culture.

To determine whether these transcriptional changes were also present in the sporadic form of the disease, the gene expression profile of SpCCM cells was analyzed relative to healthy HUVECs (**Figure 4D–F**). SpCCM cells showed a significant reduction in major endothelial identity markers, including genes involved in cell adhesion, vasoprotective function, and endothelial barrier integrity (**Figure 4D**). Simultaneously, EndMT-associated markers were overexpressed, most notably *FN1, αSMA,* and *FSP1*, the latter showing a particularly striking increase (**Figure 4E**). Regarding cellular homeostasis, alterations were detected in markers of proliferation, inflammation, and antioxidant response, consistent with the findings in familial CCM, although the magnitude of these changes was generally smaller in SpCCM than in FCCM (**Figure 4F**).

Altogether, these results suggest that both forms of the disease share a similar molecular profile, with sporadic cavernoma cells appearing to be at a somewhat less advanced stage of EndMT.

Figure 4. Differential gene expression in FCCM and SpCCM by RT-qPCR. Results obtained using BioRad's iQ5 Optical System software, with 18S as the housekeeping gene, for FCCM (blue titles) and SpCCM (black titles). (A–C) FCCM: control BOECs versus cavernoma cells at subculture passages 5 and 11, to assess changes over time. Expression of genes related to endothelial identity (A), endothelial-to-mesenchymal transition (B), and other cellular functions (C). (D–F) SpCCM: control HUVECs as the reference condition. Expression of genes related to endothelial identity (D), endothelial-to-mesenchymal transition (E), and other cellular functions (F). Error bars denote ± SD. Two-way ANOVA with Tukey's multiple comparisons test. *p<0.05, **p<0.01, ***p<0.001, ****p<0.0001.

Protein Analysis by Western Blot and Immunofluorescence shows loss of endothelial markers in FCCM and SpCCM cells

To assess the status of the actin and tubulin cytoskeleton, as well as the expression and localization of key endothelial identity proteins, an immunofluorescence assay was performed. FCCM cells displayed a markedly disorganized actin cytoskeleton, dominated by stress fibers, with a clear loss of the typical polygonal endothelial morphology. Tubulin organization, in contrast, did not differ substantially between FCCM and control cells. Regarding endothelial markers, FCCM cells showed reduced CD31 and VE-cadherin immunostaining. CD31 in particular, which localizes to intercellular junctions in control BOECs, showed a marked decrease in both abundance and junctional localization, reinforcing the loss of endothelial identity already observed in the functional and transcriptional assays **(Figure 5A)**. A similar pattern was observed in SpCCM cells, with a disorganized actin cytoskeleton and reduced CD31 expression comparable to that seen in FCCM **(Figure 5B)**.

To assess KRIT1 protein expression, Western blot analysis was performed in FCCM cells. Analysis of CCM2 protein was not performed in SpCCM cells because the somatic mutations are present in only a small fraction of the cultured cells, making changes in total protein levels unlikely to be detectable by Western blot. Consistent with the genetic alteration, FCCM cells showed reduced CCM1 protein levels compared with control HUVECs. **(Figure 5C)**. In SpCCM cells, VE-cadherin protein levels were reduced, further supporting the loss of endothelial identity (**Figure 5D**).

Figure 5. Protein expression analysis in FCCM and SpCCM. (A, B) Confocal immunofluorescence images. (A) Staining of endothelial markers (CD31, VE-cadherin) and cytoskeletal proteins (β-actin, γ-tubulin) in BOECs and FCCM cells. Nuclei were counterstained with DAPI. (B) Staining of β-actin and CD31 in control HUVECs and SpCCM cells. Nuclei were counterstained with DAPI. (C) Western blot analysis of CCM1 protein in FCCM and SpCCM versus control HUVECs, normalized to tubulin as loading control. Band intensity quantifications are

shown as loading-normalized ratios. (D) Western blot analysis of VE-cadherin in SpCCM, using actin as loading control. Band intensity quantifications are shown as loading-normalized ratios.

DISCUSSION

The present study identifies a continuum of endothelial dysfunction across CCM, from early alterations in apparently non-lesional KRIT1-heterozygous endothelial cells to an advanced EndMT-like phenotype in endothelial cells derived from familial and sporadic lesions.

Cerebral cavernous malformations (CCMs) occur in either sporadic or familial forms. The sporadic form affects approximately 1 in 200 individuals and does not follow a hereditary pattern, whereas familial multiple CCM is a rare disorder caused by germline mutations in *CCM1, CCM2,* or *CCM3*, which encode components of the CCM signaling complex (CSC) [33–35]. This inherited form is transmitted in an autosomal dominant manner, with a 50% risk of transmission to offspring, and may involve the central nervous system (particularly the cerebellum), the spinal cord, and even ocular structures [36–38]. In the present study, we sought to functionally and molecularly endothelial cells derived both from cavernomatous lesions and from the apparently normal vasculature of patients with familial multiple CCM.

Patient-derived endothelial cells (BOECs) were obtained by culturing circulating progenitors from peripheral blood, providing a representative vascular model in a cohort of three siblings: two carriers of a *CCM1* mutation and one wild-type for this mutation. This approach allowed us to compare wild-type endothelial cells with heterozygous endothelial cells that, despite carrying a mutation in one *CCM1* allele, do not originate from a cavernous lesion.

Comparison of the expression pattern across the three siblings showed that even endothelial cells heterozygous for *CCM1* mutations exhibit gene expression alterations, including partial loss of endothelial marker expression (**Figure 1A, Figure 2C**). These findings suggest that a single germline mutation is sufficient to induce a partially dysfunctional endothelial state, supporting our previously published results [32]. In the family studied here (two siblings affected by a *CCM1* mutation and one unaffected sibling), we also observed marked heterogeneity between the two affected individuals despite their sharing the same mutation. Endothelial morphology and function, including migration and tubulogenesis, differed substantially between them (**Figure 2A, B**), highlighting the importance of genomic background. Endothelial dysfunction was more severe in the patient who additionally carried heterozygous variants in several genes that may act as modifiers. Taken together, these results indicate that the presence of a heterozygous *KRIT1* mutation is associated with measurable alterations in endothelial phenotype and function in line with the recent report by Arce et al. [39]

While endothelial cells carrying a single *CCM1* mutation already show the initiation of endothelial-to-mesenchymal transition (EndMT), evidenced by reduced endothelial marker expression, cells derived from cavernomatous lesions (whether familial or sporadic), carry two-hit mutations in the CCM genes and display an almost complete loss of endothelial markers together with a gain of dedifferentiation markers [19,20] (**Figure 4**). These findings support an advanced EndMT-like phenotype in CCM-derived endothelial cells [27].

Furthermore, the comparison between familial and sporadic cavernomas revealed highly similar molecular profiles (**Figure 3, Figure 4**), supporting the hypothesis that both forms share common pathogenic mechanisms despite differing in their origin (germline versus somatic). This finding supports the notion that therapeutic approaches developed for one form of CCM may also be applicable to the other.

These observations, together with the fact that cell cultures derived from cavernous lesions constitute useful models for *in vitro* drug screening (including personalized screening whenever feasible using either repurposed or novel compounds), led us to explore potential therapeutic strategies for CCM.

Two major therapeutic approaches can be envisioned for CCM. The first comprises maintenance therapies aimed at halting lesion growth and reducing hemorrhagic risk. The second, more ambitious, involves curative interventions capable of reversing the malformed phenotype and restoring vascular integrity. Although the latter might eventually be achievable through targeted molecular editing potentially via nanoparticle-assisted delivery systems, it remains a long-term goal. In the short term, drug repurposing represents a more immediate avenue, using already approved compounds with the potential to stabilize CCM lesions and prevent hemorrhage. Exomic analysis of resected CCM lesions suggests that surgery is frequently required precisely when somatic activating mutations in the PI3K pathway emerge in a subset of cavernoma cells, supporting the notion that growth-prone cavernomas acquire secondary somatic *PI3KCA* mutations that drive proliferation. PI3K pathway inhibition may therefore represent a targeted therapeutic strategy.

We tested this hypothesis *in vitro* by treating endothelial cells derived from both CCM lesions with PI3K pathway inhibitors, specifically buparlisib (a direct PI3K inhibitor) and rapamycin (an mTOR inhibitor acting downstream of PI3K). Both treatments markedly reduced cellular proliferation (**Figure 6A, B**), consistent with a contribution of PI3K/mTOR signaling to CCM lesion expansion. Given its clinical availability and established safety profile, rapamycin may represent a viable maintenance therapy, particularly for patients with recurrent lesion growth requiring repeated surgery or stereotactic radiosurgery (e.g., Gamma Knife).

Figure 6. Drug treatment reduces FCCM cell viability. Brightfield images showing the progression of a viability assay with different treatments (buparlisib (A), rapamycin (B), and propranolol/ICI-118,551 (C)) at increasing concentrations on FCCM cells, showing the overall state of the culture, cell morphology, and cell death. Alongside, graphs show the cell viability based on ATP quantification; all treatments reduced culture viability. Error bars denote ± SD. Ordinary one-way ANOVA with Tukey's multiple comparisons test. *p<0.05, **p<0.01, ***p<0.001, ****p<0.0001.

We further evaluated repurposed drugs previously reported to show potential in CCM treatment. Propranolol, a non-selective β-adrenergic blocker, has progressed to a phase II clinical trial and received orphan drug designation based on its efficacy in reducing lesion burden in animal models and small human cohorts [40-42,29]. In our assays, both propranolol and ICI-118,551, a selective β2-adrenergic receptor antagonist, reduced proliferation of CCM-derived endothelial cells to a comparable extent (**Figure 6C, D**), suggesting that selective β2 blockade may be as effective as combined β1/β2 blockade with the advantage of avoiding hypertension and bradycardia, side effects of propranolol.

Other compounds that enhance vascular homeostasis have also shown efficacy in preclinical models, including antioxidants that mitigate oxidative stress, such as tempol, statins (atorvastatin, simvastatin), and inhibitors of the RhoA/ROCK signaling cascade, such as fasudil, all of which may reduce lesion burden and hemorrhage [43-45]. Our *in vitro* models provide a platform to screen these and other compounds, reinforcing and extending findings from preclinical animal studies.

Overall, our findings support a model in which endothelial dysfunction precedes and progresses toward an EndMT-like phenotype in CCM. The use of patient-derived endothelial cells provides a human model for dissecting the molecular determinants of CCM endothelial dysfunction and for evaluating candidate therapeutic strategies

STUDY LIMITATIONS

- Limited number of primary cultures from each type, heterozygous carriers, FCCM and SpCCM due to the difficulty in obtaining patient fresh samples in rare diseases
- Genetic heterogeneity among cell cultures, due to the primary origin of cultures from different patients
- In vitro nature of the experiments. No animal model, is used due to the study of real patients
- Possibility of changes associated with culture/passage due to the primary nature of cell cultures, since these cultures are not immortal and passages also mean ageing
- Viability was the only pharmacological readout, due to the preliminary screening of primary cultures with these repurposed drugs

ACKNOWLEDGEMENTS

The authors gratefully acknowledge the Spanish Cavernoma Patient Association for its continuous support and valuable collaboration throughout this research.

DISCLOSURES

The authors declare that they have no conflicts of interest.

SOURCES OF FUNDING

This work was supported by the Spanish Ministry of Science and Innovation (MICINN) through the State Research Agency (Agencia Estatal de Investigación, AEI; 10.13039/501100011033) under Grant PID2020-115371RB-I00, co-funded by the European Regional Development Fund (ERDF/FEDER), and under Grant PID2023-146593OB-I00

AUTHOR CONTRIBUTIONS: Conceptualization, M.G.-B, and L.M.B.; methodology, V.A.,M.G.-B, A.L-G., A.L., A.C., R.I.-B., A.C.-A., L.R.-P and L.M.B., software, J.V.-L.; validation, L.M.B., V.A., and A.M-C.; formal analysis, V.A., C.S.M, L.L.H, L.R.-P.; investigation; M.G.-B.,V.A., L.R.-P. R.I.-B., A.C.-A and LMB; resources, L.M.B.; data curation, M.G.-B, A.M.C., V.A., and L.M.B.; writing—original draft preparation; M.G.-B, L.M.B. and V.A.; writing—review and editing, M.G.-B., L.M.B., A.M.C., and V. A..; visualization, L.M.B and V.A.; supervision, L.M.B.; V.A., A.M.C.; project ad-ministration, L.M.B.; funding acquisition, L.M.B. All authors have read and agreed to the published version of the manuscript.

REFERENCES

1. Vernooij MW, Ikram MA, Tanghe HL, Vincent AJ, Hofman A, Krestin GP, et al. (2007) Incidental findings on brain MRI in the general population. N Engl J Med 357:1821–1828.

2. Morris Z, Whiteley WN, Longstreth WT Jr, Weber F, Lee YC, Tsushima Y, et al. (2009) Incidental findings on brain magnetic resonance imaging: systematic review and meta-analysis. BMJ 339:b3016.

3. Flemming KD, Graff-Radford J, Aakre J, Kantarci K, Lanzino G, Brown RD Jr, et al. (2017) Population-based prevalence of cerebral cavernous malformations in older adults: Mayo Clinic Study of Aging. JAMA Neurol 74:801–805.

4. Batra S, Lin D, Recinos PF, Zhang J, Rigamonti D. (2009) Cavernous malformations: natural history, diagnosis, and treatment. Nat Rev Neurol 5:659–670.

5. Awad IA, Polster SP. (2019) Cavernous angiomas: deconstructing a neurosurgical disease. J Neurosurg 131:1–13.

6. Akers A, Al-Shahi Salman R, Awad IA, Dahlem K, Flemming K, Hart B, et al. (2017) Synopsis of guidelines for the clinical management of cerebral cavernous malformations. Neurosurgery 80:665–680.

7. Cox EM, Bambakidis NC, Cohen ML. (2017) Pathology of cavernous malformations. Handb Clin Neurol 143:267–277.

8. Laberge-le Couteulx S, Jung HH, Labauge P, Houtteville JP, Lescoat C, Cecillon M, et al. (1999) Truncating mutations in CCM1, encoding KRIT1, cause hereditary cavernous angiomas. Nat Genet 23:189–193.

9. Liquori CL, Berg MJ, Siegel AM, Huang E, Zawistowski JS, Stoffer T, et al. (2003) Mutations in a gene encoding a novel protein containing a phosphotyrosine-binding domain cause type 2 cerebral cavernous malformations. Am J Hum Genet 73:1459–1464.

10. Bergametti F, Denier C, Labauge P, Arnoult M, Boetto S, Clanet M, et al. (2005) Mutations within the programmed cell death 10 gene cause cerebral cavernous malformations. Am J Hum Genet 76:42–51.

11. Zhou Z, Tang AT, Wong WY, Bamezai S, Goddard LM, Shenkar R, et al. (2016) Cerebral cavernous malformations arise from endothelial gain of MEKK3–KLF2/4 signalling. Nature 532:122–126.

12. Cuttano R, Rudini N, Bravi L, Maddaluno L, Giampietro C, Papa E, et al. (2016) KLF4 is a key determinant in the development and progression of cerebral cavernous malformations. EMBO Mol Med 8:6–24.

13. Renz M, Otten C, Faurobert E, Rudolph F, Zhu Y, Boulday G, et al. (2015) Regulation of β1 integrin–KLF2-mediated angiogenesis by CCM proteins. Dev Cell 32:181–190.

14. Gianfrancesco F, Cannella M, Martino T, Maglione V, Esposito T, Innocenzi G, et al. (2007) Highly variable penetrance in subjects affected with cavernous cerebral angiomas carrying novel CCM1 and CCM2 mutations. Am J Med Genet B Neuropsychiatr Genet 144B:691–695.

15. Zafar A, Quadri SA, Farooqui M, Ikram A, Robinson M, Hart BL, et al. (2019) Familial cerebral cavernous malformations. Stroke 50:1294–1301.

16. Denier C, Labauge P, Brunereau L, Cavé-Riant F, Marchelli F, Arnoult M, et al. (2004) Clinical features of cerebral cavernous malformations patients with KRIT1 mutations. Ann Neurol 55:213–220.

17. Snellings DA, Girard R, Lightle R, Moore T, Sheth SA, Li L, et al. (2022) Developmental venous anomalies are a genetic primer for cerebral cavernous malformations. Nat Cardiovasc Res 1:246–252.

18. Gault J, Awad IA, Recksiek P, Shenkar R, Breeze R, Handler M, et al. (2009) Cerebral cavernous malformations: somatic mutations in vascular endothelial cells. Neurosurgery 65:138–145.

19. McDonald DA, Shi C, Shenkar R, Gallione CJ, Akers AL, Li S, et al. (2014) Lesions from patients with sporadic cerebral cavernous malformations harbor somatic mutations in the CCM genes. Hum Mol Genet 23:4357–4370.

20. Akers AL, Johnson E, Steinberg GK, Zabramski JM, Marchuk DA. (2009) Biallelic somatic and germline mutations in cerebral cavernous malformations. Hum Mol Genet 18:919–930.

21. Hong T, Xiao X, Ren J, Cui B, Zong Y, Zou J, et al. (2021) Somatic MAP3K3 and PIK3CA mutations in sporadic cerebral and spinal cord cavernous malformations. Brain 144:2648–2658.

22. Ren AA, Snellings DA, Su YS, Hong CC, Castro M, Tang AT, et al. (2021) PIK3CA and CCM mutations fuel cavernomas through a cancer-like mechanism. Nature 594:271–276.

23. Peyre M, Miyagishima D, Bielle F, Chapon F, Sierant M, Venot Q, et al. (2021) Somatic PIK3CA mutations in sporadic cerebral cavernous malformations. N Engl J Med 385:996–1004.

24. Weng J, Yang Y, Song D, Huo R, Li H, Chen Y, et al. (2021) Somatic MAP3K3 mutation defines a subclass of cerebral cavernous malformation. Am J Hum Genet 108:942–950.

25. Ren J, Huang Y, Ren Y, Tu T, Qiu B, Ai D, et al. (2023) Somatic variants of MAP3K3 are sufficient to cause cerebral and spinal cord cavernous malformations. Brain 146:3634–3647.

26. Huo R, Yang Y, Sun Y, Zhou Q, Zhao S, Mo Z, et al. (2023) Endothelial hyperactivation of mutant MAP3K3 induces cerebral cavernous malformation enhanced by PIK3CA gain-of-function mutation. Angiogenesis 26:295–312.

27. Maddaluno L, Rudini N, Cuttano R, Bravi L, Giampietro C, Papa E, et al. (2013) EndMT contributes to the onset and progression of cerebral cavernous malformations. Nature 498:492–496.

28. Li L, Ren AA, Gao S, Su YS, Yang J, Bockman J, et al. (2023) mTORC1 inhibitor rapamycin inhibits growth of cerebral cavernous malformation in adult mice. Stroke 54:2906–2917.

29. Dulamea AO, Lupescu IC. (2024) Cerebral cavernous malformations—an overview on genetics, clinical aspects and therapeutic strategies. J Neurol Sci 461:123044.

30. Ren J, Wang D, Wang L, Jiang C, Tian A, Cui Z, et al. (2025) Clinical, genomic, and histopathologic diversity in cerebral cavernous malformations. Acta Neuropathol Commun 13:23.

31. Chohan MO, Marchio S, Morrison LA, Sidman RL, Cavenee WK, Awad IA. (2019) Emerging pharmacologic targets in cerebral cavernous malformation. JAMA Neurol 76:492–500.

32. Lorente-Herraiz L, Cuesta AM, Granado J, Recio-Poveda L, Botella LM, Albiñana V. (2024) Molecular and cellular characterization of primary endothelial cells from a familial cavernomatosis patient. Int J Mol Sci 25:3952.

33. Labauge P, Denier C, Bergametti F, Tournier-Lasserve E. (2007) Genetics of cavernous angiomas. Lancet Neurol 6:237–244. https://doi.org/10.1016/S1474-4422(07)70053-4

34. Boulday G, Blécon A, Petit N, Chareyre F, Garcia LA, Niwa-Kawakita M, et al. (2009) Tissue-specific conditional CCM2 knockout mice establish the essential role of endothelial CCM2 in angiogenesis: implications for human cerebral cavernous malformations. Dis Model Mech 2:168–177. https://doi.org/10.1242/dmm.001263

35. Draheim KM, Fisher OS, Boggon TJ, Calderwood DA. (2014) Cerebral cavernous malformation proteins at a glance. J Cell Sci 127:701–707.

36. Rigamonti D, Drayer BP, Johnson PC. (1989) The natural history of cavernous malformations. J Neurosurg 71:825–831.

37. Whitehead KJ, Chan AC, Navankasattusas S, Koh W, London NR, Ling J, et al. (2009) The cerebral cavernous malformation signaling pathway promotes vascular integrity via Rho GTPases. Nat Med 15:177–184.

38. Stockton RA, Shenkar R, Awad IA, Ginsberg MH. (2010) Cerebral cavernous malformations proteins inhibit Rho kinase to stabilize vascular integrity. J Exp Med 207:881–896.

39. Arce M, Erzar I, Yang F, Senthilkumar N, Onyeogaziri FC, Ronchi D, et al. (2025) KRIT1 heterozygous mutations are sufficient to induce a pathological phenotype in patient-derived iPSC models of cerebral cavernous malformation. Cell Rep 44:115576.

40. Oldenburg J, Malinverno M, Globisch MA, Maderna C, Corada M, Orsenigo F, et al. (2021) Propranolol reduces the development of lesions and rescues barrier function in cerebral cavernous malformations: a preclinical study. Stroke 52:1418–1427.

41. Li DY, Whitehead KJ. (2010) Evaluation of pharmacological therapies for CCM. Trends Mol Med 16:447–456.

42. Lanfranconi S, Scola E, Meessen JMTA, Pallini R, Bertani GA, Al-Shahi Salman R, et al. (2023) Safety and efficacy of propranolol for treatment of familial cerebral cavernous malformations (Treat_CCM): a randomised, open-label, blinded-endpoint, phase 2 pilot trial. Lancet Neurol 22:35–44.

43. McDonald DA, Shi C, Shenkar R, Stockton RA, Liu F, Ginsberg MH, et al. (2012) Fasudil decreases lesion burden in CCM murine models. Stroke 43:571–574.

44. Borikova AL, Dibble CF, Sciaky N, Welch CM, Abell AN, Bencharit S. (2010) Rho kinase inhibition rescues the endothelial cell cerebral cavernous malformation phenotype. J Biol Chem 285:11760–11764.

45. Stockton RA, et al. (2010) CCM pathogenesis and ROCK inhibition. Circ Res 106:920–928.

A)

Sample	Gene	Region	Variant	Frequency	Protein effect
BOEC-A ***BOEC-B***	*KRIT1*	chr7:91843920 **Intrón 15**	c.1730+5G>A (NM_194454.3) **rs1563244618**	**A**: 52% **B**: 46%	**Disrupts the splice donor site**
	MPL	chr1:43805713 **Exón 5**	c.769C>T p.Arg257Cys (NM_005373.3) **rs121913611**	**A**: 49% **B**: 52%	p.Arg257Cys **Missense**
BOEC-A	*F11R*	chr1:160970066 **Exón 5**	c.461C>G p.Ser154Ter (NM_016946.6)	56%	p.Ser154Ter **Stop codon**
	RIF1	chr2:152308220 **Intrón 21**	c.2344+1G>T (NM_018151.5)	46%	**Disrupts the splice donor site**
	ALDH1A2	chr15:58257975 **Exon 8**	c.847_848dup p.Thr284Ter (NM_003888.4)	44%	p.Thr284Ter **Stop codon**
	AREL1	chr14:75134298 **Intron 15**	c.1915-1G>A (NM_001039479.2)	59%	**Disrupts the splice acceptor site**
BOEC-B	*SMAD2*	chr18:45372041 **Exon 9**	c.1085_1128del	5,37%	p.Cys362Serfs*5 **Frameshift**
BOEC-C	**CONTROL (WT)**				
FCCM	*KRIT1*	chr7:91830749 **Intron 19**	c.2026-12A>G (NM_194454.3) **rs1041438637**	47% (Germinal)	**Cryptic splice acceptor site**
	KRIT1	chr7:91871403 **Exon 4**	c.47G>A p.Arg16Hi (NM_194454.3)	62%	p.Arg16His **Missense**
	PIK3CA	chr3:178936082 **Exon 10**	c.1624G>A, p.Glu542Lys (NM_006218.3)	5,88%	p.Glu542Lys **Missense**
SpCCM	*CCM2*	chr7:45077888 **Exon 2**	c.67A>T (NM_031443.4)	4,69%	p.Lys23* **Nonsense**
	CCM2	chr7:45109514 **Exon 6**	c.702del (NM_031443.4)	2,70%	p.Phe234Leufs*58 **Frameshift**
	PIK3CA	ch3:178952085 **Exon 26**	c.3140A>G (NM_006218.4) **rs121913279**	4,25%	p.His1047Arg **Missense**

B)

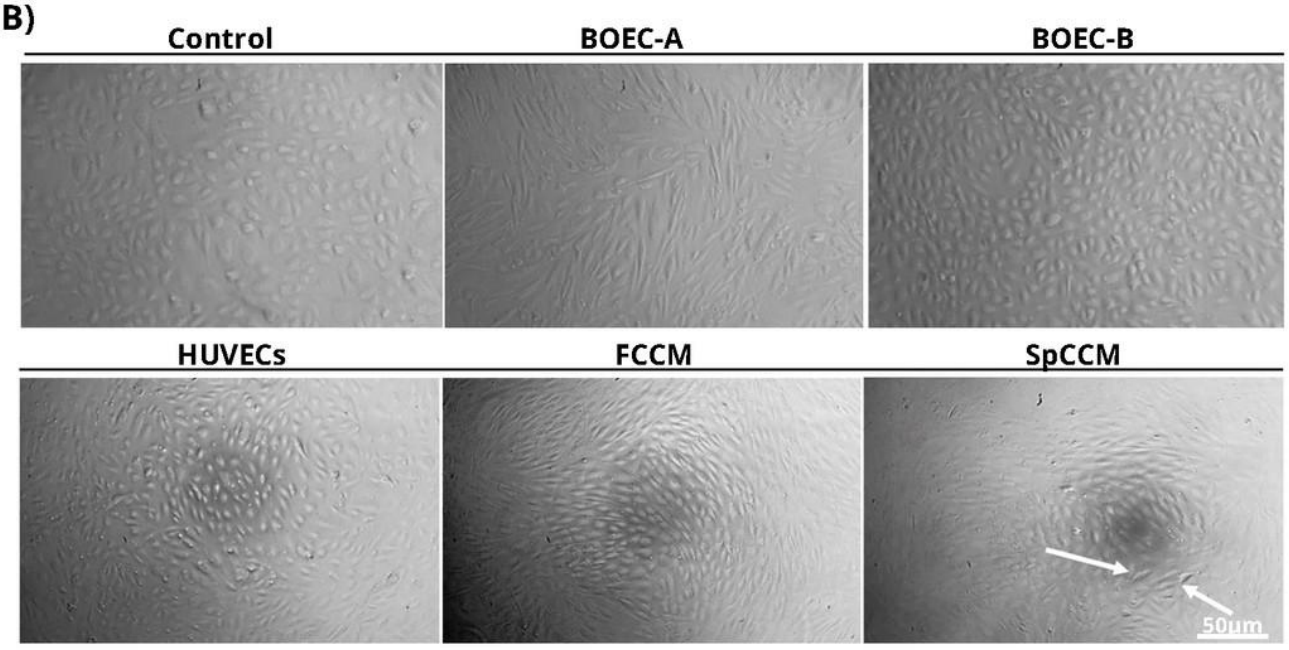


Figure 1. Genetic and morphological characterization of patient-derived endothelial cells. (A) Variants identified by whole-exome sequencing (500×) in BOEC-A and BOEC-B, FCCM, and SpCCM cells. Variants shared by BOEC-A and BOEC-B are shown first, followed by variants identified exclusively in each sample. The table includes the gene, genomic region, variant, allele frequency, and predicted protein effect. (B) Representative brightfield images of BOEC cultures from the three siblings (Control, BOEC-A, and BOEC-B, upper row) and FCCM and SpCCM cells compared with control HUVECs (lower row).

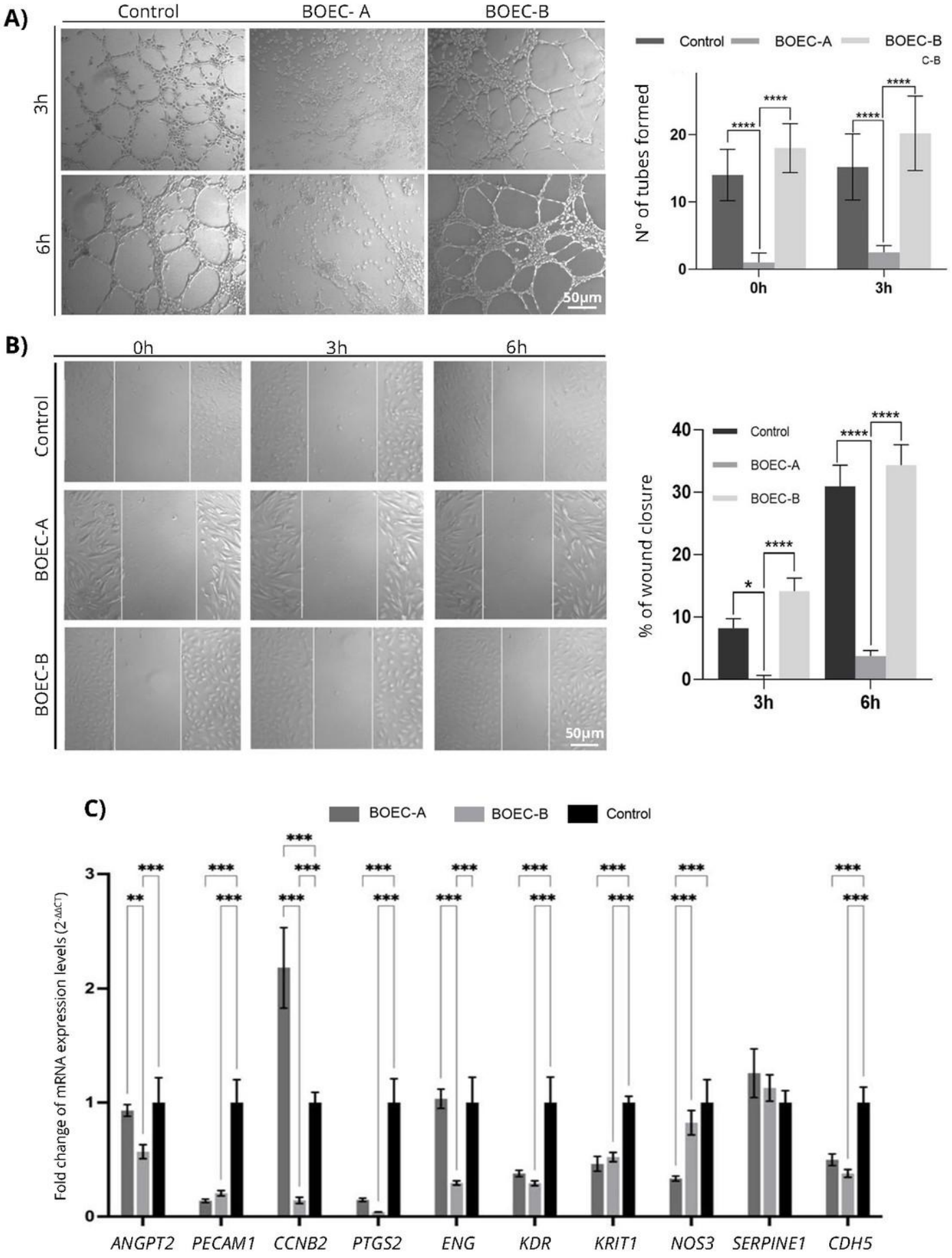


Figure 2. Functional characterization of BOECs A, B, and C. A) Tubulogenesis assay. Brightfield images show tube formation by the different cell types, and the graph shows the number of closed tubes formed by each cell type over time. Error bars denote ± SD. Two-way ANOVA with Tukey's multiple comparisons test. ****p<0.0001. (B) Wound healing assay. Brightfield images show the progression of wound closure, with vertical lines indicating the position of the wound front. The graph on the right shows the percentage of wound closure over time. Error bars denote ± SD. Two-way ANOVA with Sidak's multiple comparisons test. *p<0.05, ****p<0.0001. (C) RT-qPCR analysis performed using Bio-Rad iQ5 Optical System software, with *18S* as the housekeeping gene. Differential expression was observed in genes involved in endothelial function, cell cycle regulation, and inflammation. Error bars denote ± SD. Two-way ANOVA with Tukey's multiple comparisons test. *p<0.05, **p<0.01, ***p<0.001, ****p<0.0001.

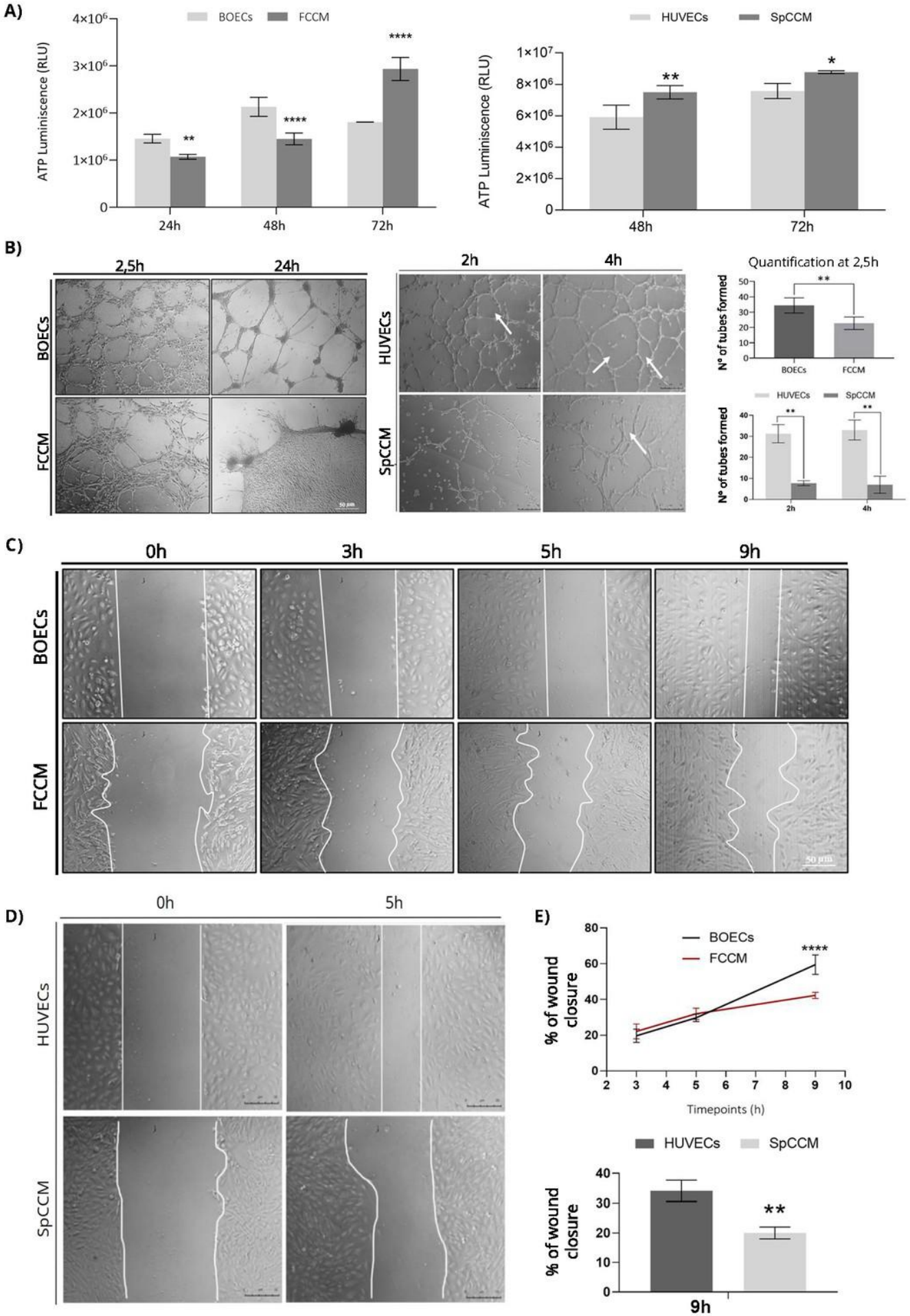


Figure 3. Functional characterization of FCCM and SpCCM cells. (A) Cell viability assessed by ATP quantification over time in FCCM cells compared with control BOECs (left) and SpCCM cells compared with control HUVECs (right). Error bars indicate ± SD. Two-way ANOVA with Šídák's multiple-comparisons test. *p<0.05; **p<0.01; ***p<0.001; ****p<0.0001. (B) Representative brightfield images of the tubulogenesis assay comparing control BOECs and FCCM cells (left) and control HUVECs and SpCCM cells (right) at the indicated time points. Quantification of closed tubes is shown on the right. Upper graph: control BOECs versus FCCM cells at 2.5 h, as tubes had retracted by 24 h. Error bars indicate ± SEM. Welch's t-test. **p<0.01. Lower graph: control HUVECs versus SpCCM cells at 2 and 4 h. Error bars indicate ± SD. Two-way ANOVA with Šídák's multiple-comparisons test. **p<0.01. (C) Representative brightfield images of the wound healing assay comparing control BOECs and FCCM cells at 0, 3, 5, and 9 h. Vertical lines indicate the wound edges. (D) Representative brightfield images comparing control HUVECs and SpCCM cells at 0 and 5 h. Vertical lines indicate the wound edges. (E) Quantification of wound closure. Upper graph: percentage of wound closure over time in control BOECs and FCCM cells. Error bars indicate ± SD. Two-way ANOVA with Šídák's multiple-comparisons test. ****p<0.0001. Lower graph: percentage of wound closure in control HUVECs and SpCCM cells at 9 h. Error bars indicate ± SD. Unpaired t-test with Welch's correction. **p<0.01.

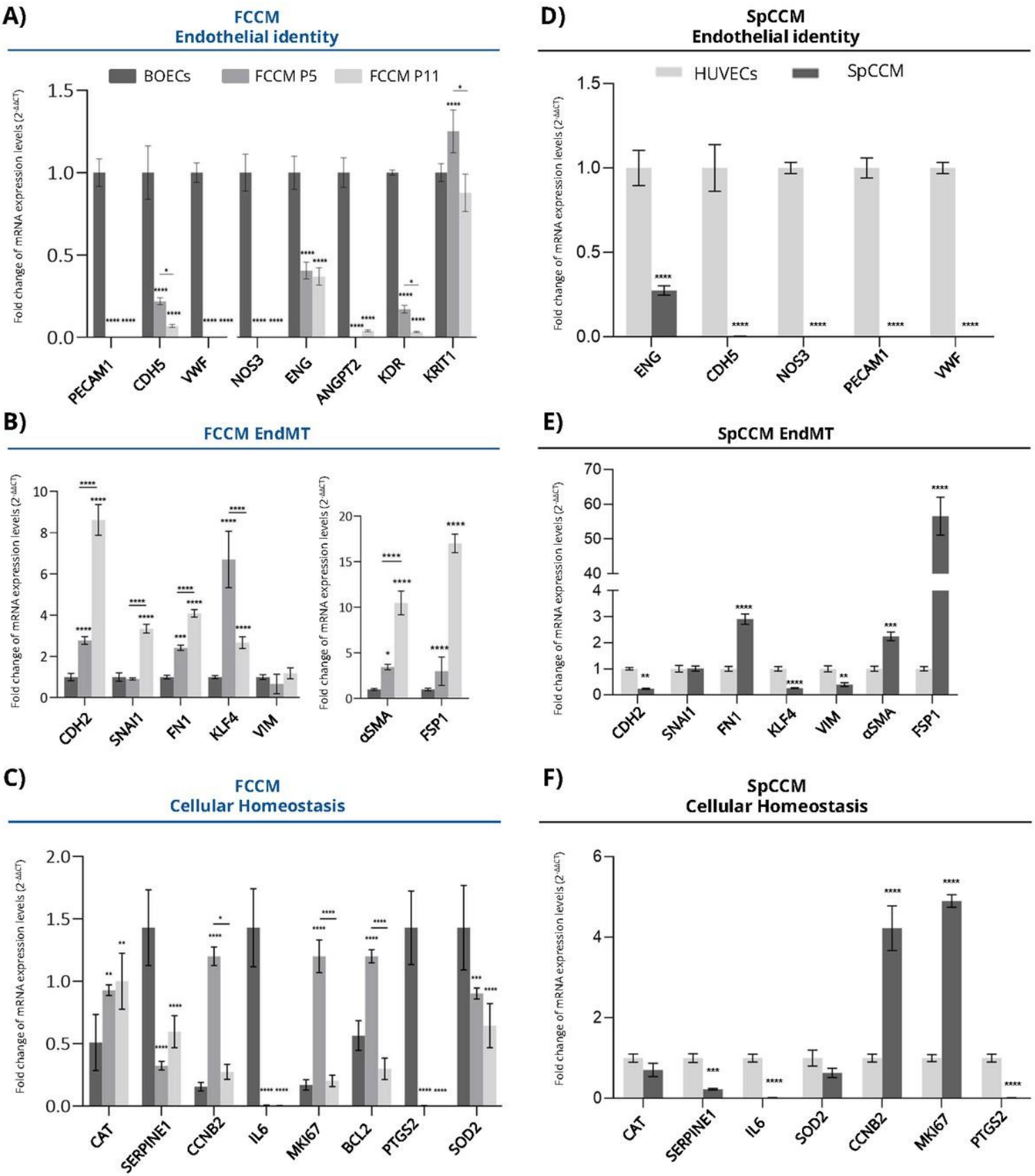


Figure 4. Differential gene expression in FCCM and SpCCM by RT-qPCR. Results obtained using BioRad's iQ5 Optical System software, with 18S as the housekeeping gene, for FCCM (blue titles) and SpCCM (black titles). (A–C) FCCM: control BOECs versus cavernoma cells at subculture passages 5 and 11, to assess changes over time. Expression of genes related to endothelial identity (A), endothelial-to-mesenchymal transition (B), and other cellular functions (C). (D–F) SpCCM: control HUVECs as the reference condition. Expression of genes related to endothelial identity (D), endothelial-to-mesenchymal transition (E), and other cellular functions (F). Error bars denote ± SD. Two-way ANOVA with Tukey's multiple comparisons test. *p<0.05, **p<0.01, ***p<0.001, ****p<0.0001.

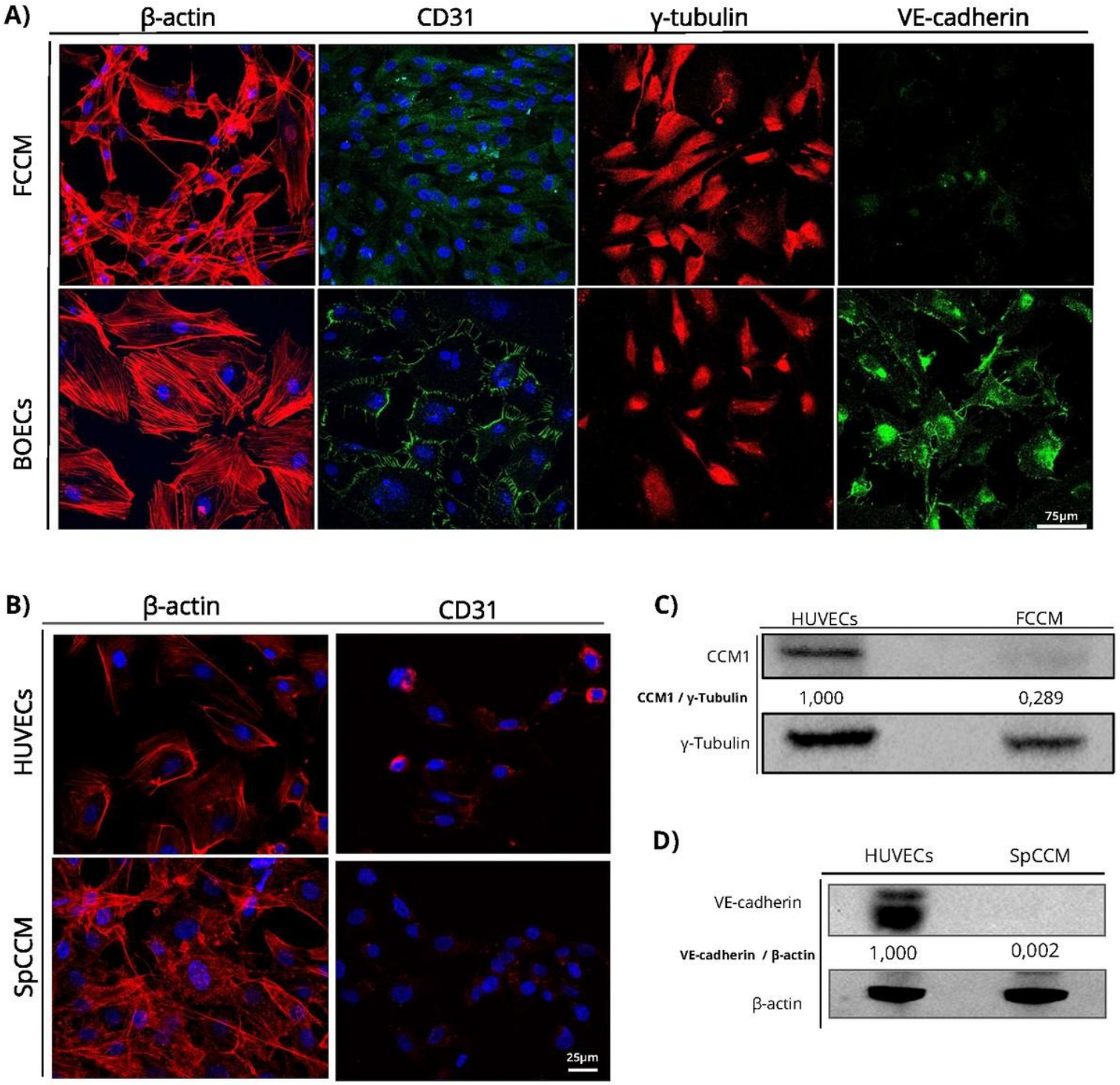


Figure 5. Protein expression analysis in FCCM and SpCCM. (A, B) Confocal immunofluorescence images. (A) Staining of endothelial markers (CD31, VE-cadherin) and cytoskeletal proteins (β-actin, γ-tubulin) in BOECs and FCCM cells. Nuclei were counterstained with DAPI. (B) Staining of β-actin and CD31 in control HUVECs and SpCCM cells. Nuclei were counterstained with DAPI. (C) Western blot analysis of CCM1 protein in FCCM and SpCCM versus control HUVECs, normalized to tubulin as loading control. Band intensity quantifications are shown as loading-normalized ratios. (D) Western blot analysis of VE-cadherin in SpCCM, using actin as loading control. Band intensity quantifications are shown as loading-normalized ratios.

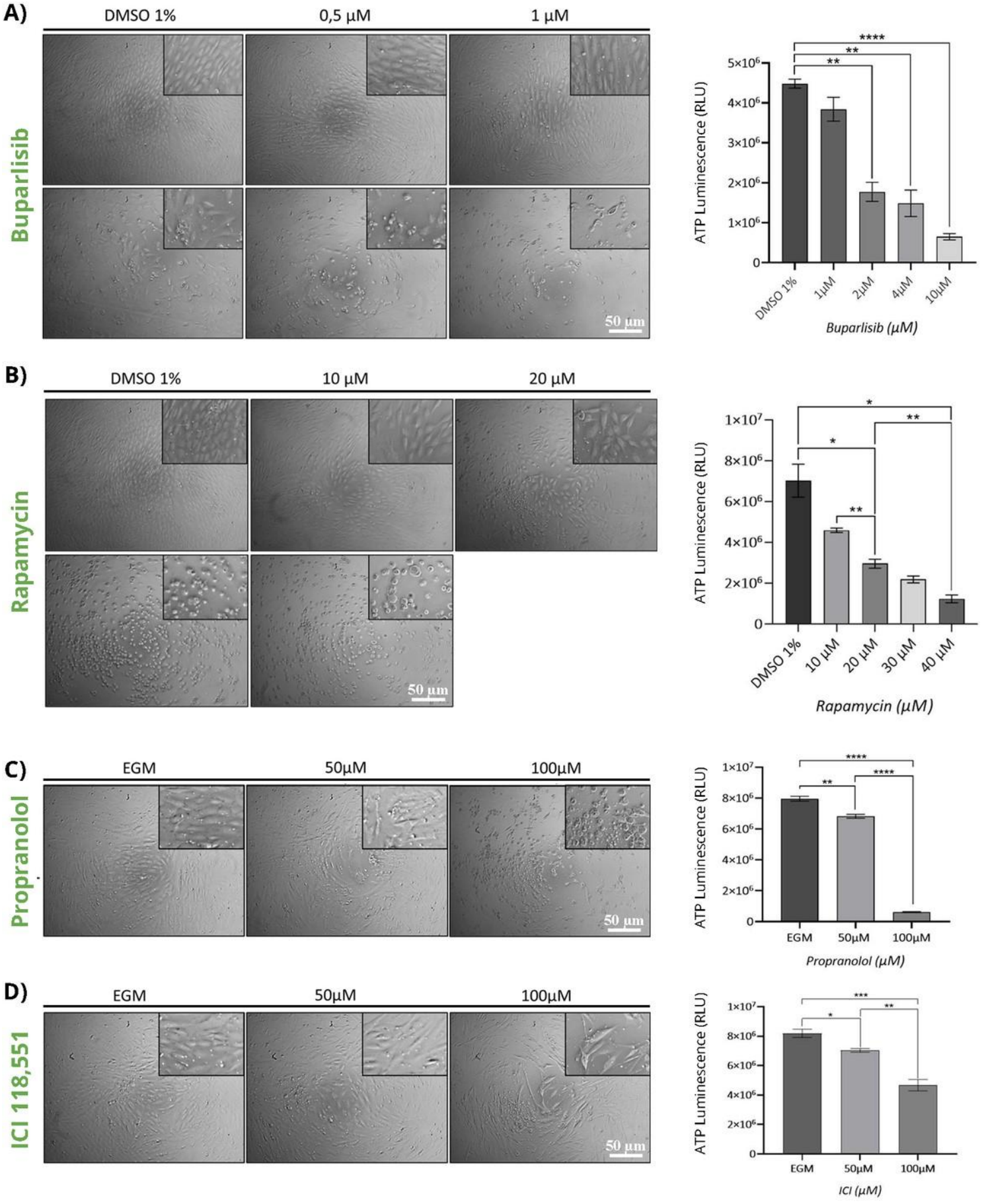


Figure 6. Drug treatment reduces FCCM cell viability. Brightfield images showing the progression of a viability assay with different treatments (buparlisib (A), rapamycin (B), and propranolol/ICI-118,551 (C)) at increasing concentrations on FCCM cells, showing the overall state of the culture, cell morphology, and cell death. Alongside, graphs show the cell viability based on ATP quantification; all treatments reduced culture viability. Error bars denote ± SD. Ordinary one-way ANOVA with Tukey's multiple comparisons test. *p<0.05, **p<0.01, ***p<0.001, ****p<0.0001.